JGR Solid Earth

RESEARCH ARTICLE
10.1029/2018JB017128

Variation in Magnetic Fabrics at Low Shock Pressure Due to Experimental Impact Cratering

Amar Agarwal[1], Agnes Kontny[2], Thomas Kenkmann[1], and Michael H. Poelchau[1]

[1]Institut für Geo- und Umweltnaturwissenschaften, Albert-Ludwigs-Universität Freiburg, Freiburg, Germany, [2]Institute of Applied Geosciences, Karlsruhe Institute of Technology, Karlsruhe, Germany

Key Points:
- Experimental impact cratering in foliated Maggia gneiss imparts low shock pressure <2 GPa in crater subsurface
- The kinking and intergranular fractures in biotite change the position of magnetite grains with respect to each other
- The susceptibility increases and magnetic fabrics reorient at low shock pressures

Supporting Information:
- Supporting Information S1

Correspondence to:
A. Agarwal,
amar@daad-alumni.de

Citation:
Agarwal, A., Kontny, A., Kenkmann, T., & Poelchau, M. H. (2019). Variation in magnetic fabrics at low shock pressure due to experimental impact cratering. *Journal of Geophysical Research: Solid Earth*, *124*. https://doi.org/10.1029/2018JB017128

Received 6 DEC 2018
Accepted 8 JUL 2019
Accepted article online 12 JUL 2019

Abstract Magnetic fabrics provide important clues for understanding impact cratering processes. However, only a few magnetic fabric studies for experimentally shocked material have been reported so far. In the framework of MEMIN (Multidisciplinary Experimental and Modeling Impact Research Network), we conducted two impact experiments on blocks of Maggia gneiss with the foliation oriented perpendicular (A38) and parallel (A37) to the target surface. Maggia gneiss has plenty of biotite bands forming a strong rock foliation. The bulk magnetic susceptibility varies from 0.376×10^{-3} to 1.298×10^{-3} SI in unshocked and from 0.443×10^{-3} to 3.940×10^{-3} SI in shocked gneiss. The thermomagnetic curves reveal a Verwey transition at −147 °C and a Curie temperature between 576 and 579 °C in unshocked and shocked samples, indicating nearly pure magnetite, which carries the magnetic fabrics. In A37 and A38 kinking is prominent from the point source down to a depth of 2 and 4.2 d_p (projectile diameter) or 1 and 2.1 cm, respectively. Kinking, folding, and fracturing changed the position of magnetite grains with respect to each other to reorient the magnetic fabrics. Reorientation of magnetic fabrics is conspicuous down to 20 d_p (10 cm) in A38, where no other impact-related deformation is visible. The reorientation of magnetic fabrics may, therefore, aid in identifying impact processes at very low pressures, starting at 0.1 GPa, when other common indicators are absent.

1. Introduction

Impact cratering is one of the most important processes that has modified the extraterrestrial landscape and has been the cause of at least one mass extinction (e.g., Alvarez et al., 1980; Neukum et al., 2001; Strom et al., 2005). The passage of impact generated shock waves through target rocks causes various types of irreversible deformation, known as shock metamorphism (e.g., Grieve et al., 1996; Stöffler, 1971; Stöffler et al., 1972, 1992, 2018), as well as brittle failure (e.g., Kenkmann et al., 2014; Kumar & Kring, 2008; Winkler et al., 2018). Microscopic shock features in different minerals have successfully been quantified and calibrated with respect to the level of shock (e.g., French & Koeberl, 2010; Fritz et al., 2017; Stöffler & Langenhorst, 1994). An important tool to further our understanding of shock-induced changes in the rock comes from the study of the magnetic fabrics of minerals and rocks.

The anisotropy of magnetic susceptibility (AMS) has been commonly used to determine the petrofabric (e.g., Borradaile & Henry, 1997; Cullity & Graham, 2011; Tarling & Hrouda, 1993). Changes in the petrofabric or the mineralogy due to processes such as hydrothermal alteration, tectonic, and diagenetic stresses influence the AMS (e.g., Borradaile & Jackson, 2010; Borradaile & Werner, 1994; Hirt et al., 1993; Kapička, 1988). AMS has been successfully employed to distinguish the shock stages in L Chondrites (Gattacceca et al., 2005). AMS has also been used to reconstruct the geometry of the Sudbury impact structure (Cowan, 1999; Hirt et al., 1993), to determine the emplacement mechanism of the Chicxulub suevites (Delgadillo-Peralta et al., 2015) and to investigate the internal structure of the central uplift of the Araguainha complex impact structure, Brazil (Yokoyama et al., 2012). Based on AMS data, Misra et al. (2010) suggested an oblique impact at Lonar crater, India. Furthermore, AMS investigations have been used to reveal the peak shock pressures experienced by the target crystalline rocks of the Lockne impact structure, Sweden, and Lonar impact structure, India (Agarwal et al., 2015; Agarwal, Kontny, Srivastava, & Greiling, 2016). The necessity to understand carrier minerals is a general prerequisite for interpreting AMS fabrics and has been known long before these impact-related studies (e.g., Borradaile & Henry, 1997; Tarling & Hrouda, 1993).

The above synopsis establishes AMS as an important tool to understand the impact cratering processes. However, there have been just a few investigations on the variation in shape, anisotropy degree and

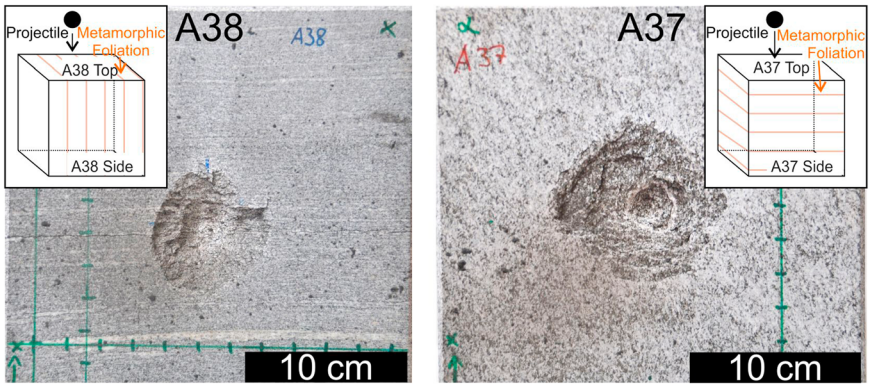

Figure 1. Photographs demonstrating the craters formed after the impact experiments. Note the difference in size and depth of the craters, and slope of the crater walls.

orientation of magnetic fabrics with the magnitude of the peak shock pressures, and the direction of shock wave propagation (e.g., Gattacceca et al., 2007; Nishioka et al., 2007). Moreover, the largest volume of the rocks at an impact structure experience low shock pressure <3 GPa (e.g., Pierazzo & Melosh, 2000). The effect of low shock pressure on magnetic minerals that cause variation in the magnetic properties has not yet been systematically investigated. In recent years there have been few studies, but only at higher shock pressures, >5 GPa (e.g., Mang et al., 2013; Reznik et al., 2016, 2017). In summary, the present study fills a gap in our knowledge on the variation of magnetic properties at low shock pressure.

Here we present impact cratering experiments on strongly foliated and highly anisotropic Maggia gneiss that were conducted in the framework of MEMIN, the Multidisciplinary Experimental and Modeling Impact Crater Research Network (Kenkmann et al., 2018). The experimental impact is expected to cause plastic deformation, such as kinking and fracturing in biotite, in crater subsurface (e.g., Cummings, 1965; Hörz, 1969; Hörz & Ahrens, 1969). The plastic deformation would vary with distance from the crater and is expected to affect the magnetic fabrics.

This spatially resolved AMS investigation of the shocked samples is devoted to understand the change in the magnetic fabrics in the target subsurface, with distance from the experimental point of impact. The second objective is to compare the magnetic fabrics below the crater floor and at the target surface with foliation parallel and perpendicular to the impact. The variation in magnetic fabrics is used as a proxy to estimate plastic deformation. The study uses microscopic evidence to propose that kinking and fracturing in biotite changed the position of magnetite grains with respect to each other to alter the magnetic fabrics.

2. Material and Methods

2.1. Target Material

Maggia gneiss was selected as the natural material for the experiments. Its type locality is the Valle Maggia, Switzerland. It is a dark gray, medium- to coarse-grained (grain size 1–3 mm) rock. It has ~50% plagioclase, ~40% biotite, and ~8% quartz. Pyroxene muscovite, epidote, and apatite are accessory. Plagioclase and biotite form mm sized subhedral grains. Fine magnetite particles (<20 μm) are sporadically distributed within the biotite. Secondary minerals indicating weathering or hydrothermal alteration are absent. In general, the grain boundaries are sharp and well defined, which further precludes alteration. Maggia gneiss has a density of 2.78 g/cm^3 (Poelchau et al., 2016). It has low porosity and well-developed metamorphic foliation, which is very homogeneous and planar throughout the target blocks and provides a profound heterogeneity and material contrast in the layering. The metamorphic lineation is not very prominent. The gneissic layers are 1–2 mm thick and thus smaller than the diameter of the projectile as well as an order of magnitude smaller than the expected crater depths and diameters (Figures 1 and 2). Brazilian disc tensile experiments, carried out parallel and perpendicular to the gneiss layering, show little difference at 7.0 ± 2.2 and 7.1 ± 1.2 MPa, respectively (Poelchau et al., 2016). The Maggia gneiss has average bulk magnetic susceptibility of

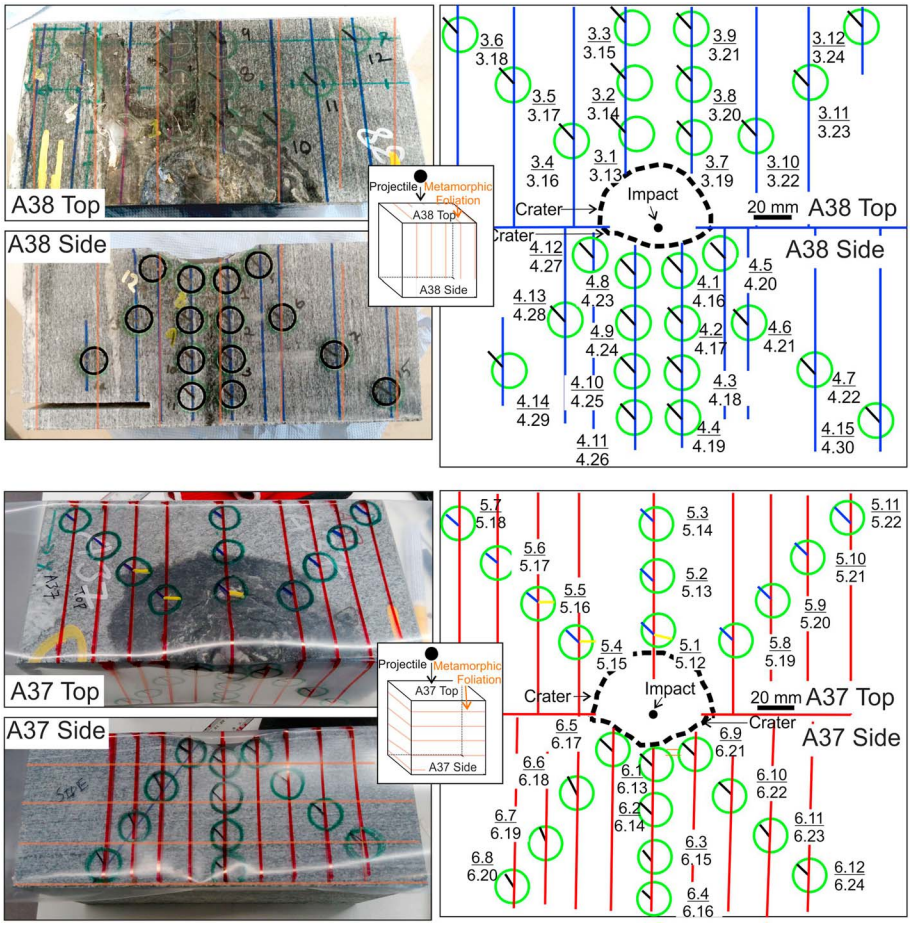

Figure 2. The photographs and sketches show the drilling position with respect to the impact crater. The black circles in the center of the sketch mark the estimated point of impact. The green circles represent the exact position of the drilled cores, and the half-arrows mark the "north" of the specimen coordinate systems. From each core, two specimens were cut. The upper and lower specimens are written as nominator and denominator of the fraction. The foliation in Experiment A38 was oriented parallel to the impact direction, while the foliation in A37 was perpendicular to the impact direction. The blocks are 20 × 10 × 20 cm (L × B × H) in size.

0.61×10^{-3} SI indicating a dominance of paramagnetic minerals and a small contribution of ferromagnetic components (section 3.4.1). Thermomagnetic curves identified transition temperatures indicative of almost pure magnetite, in small amount (section 3.3).

2.2. Experimental Cratering Setup

Two cubes of Maggia gneiss with 25-cm-long edges were used for impact cratering experiments. In one experiment (A37) the impact occurred perpendicular to the target foliation. In other words: the foliation was parallel to the target surface. In the second experiment (A38) the foliation was perpendicular to the target surface and parallel to the impact trajectory (Figure 1). Impact experiments were carried out with a two-stage light-gas gun with an 8.5-mm caliber launch tube at the Fraunhofer Ernst-Mach-Institute for High-Speed Dynamics (EMI) in Freiburg (EMI), Germany. Aluminium spheres, 0.177 g in weight and 5 mm in diameter, were used as projectiles. The projectiles were accelerated to 7.236 and 6.925 km/s, and the target chamber pressure was 1.7 and 1.9 mbar during the experiment on A38 and A37, respectively. The differences in projectile velocity are expected to not affect the subsurface deformation (Winkler et al., 2018). For details of the accelerator and the exact experimental assembly, refer to Schneider and Schäfer (2001), Poelchau et al. (2013), and Kenkmann et al. (2018). See supporting information Text S1 for detailed methodology of microscopic procedure.

2.3. Rock Magnetic Measurements

A nonmagnetic diamond bit, 14 mm in diameter, was used to drill oriented cylindrical cores from the unshocked and the two shocked gneiss blocks. Eleven (specimen 1.1 to 1.10 including 1.9B) and eight (specimen 2.1 to 2.8) specimens were drilled parallel and perpendicular to the metamorphic foliation in the unshocked blocks (Figure S2). The specimens are 14 mm in diameter and 11.2 mm long.

From sample A38, 12 cores were drilled into the target surface and 15 cores were drilled into the sawed surface, respectively (Figure 2). A prominent shock-induced fracture runs across the middle of the sample. The cores were, therefore, drilled as to avoid the fracture. Two specimens were cut from each core. Specimens 3.1 to 3.12 and 4.1 to 4.15 are from the top part of the cylinders, while specimens 3.13 to 3.24 and 4.16 to 4.30 are from the bottom part of the cylinder.

From sample A37, 11 cores were drilled in a radial pattern into the target and 12 into the sawed surface, respectively. The cores were then cut into two specimens each, producing 22 (5.1 to 5.22) and 24 (6.1 to 6.24) specimens (Figure 2). Specimens 5.1 to 5.11 and 6.1 to 6.12 are from the top part of the cores, while 5.12 to 5.22 and 6.13 to 6.24 are from the bottom part of the cores.

See supporting information Text S2 for detailed methodology of the routine thermomagnetic and magnetic fabric measurements (Hrouda, 1994; Hrouda et al., 1997; Jelinek, 1981). Confidence ellipses are calculated for the principal magnetic susceptibility axes. In shocked samples, a higher deviation would, therefore, be owed to impact processes and a lesser deviation to the inherent characteristic of the sample.

Measuring the AMS at low temperature (LT-AMS) enhances the paramagnetic fabric, and aids in its characterization (e.g., Biedermann et al., 2014; Issachar et al., 2016; Martín-Hernández & Ferré, 2007). In rocks with low ferrimagnetic component relative to the paramagnetic component, the paramagnetic minerals govern the susceptibility changes at low temperatures (Martín-Hernández & Ferré, 2007). According to Curie-Weiss law the volume susceptibility *(k)* increases as temperature *(T)* decreases as $k = C/(T - \theta)$, where C is the Curie constant, which is mineral specific and θ is the paramagnetic Curie temperature, which is 0 for pure paramagnetic materials (e.g., Cullity & Graham, 2011). Measurement of LT-AMS demands placement of extremely cold sample in the sample holder, which leads to cold air convection and drift of the electrical components, causing significant errors in LT-AMS (e.g., Issachar et al., 2016). This was avoided by placing a thin silicone sheet (1.5 mm thick) around and at the bottom of the measuring coil (e.g., Issachar et al., 2016). The kappabridge measures AMS in four steps. To keep the sample at a temperature around −196 °C, the samples were cooled for about 50 min in liquid nitrogen before each step. p_{77} is determined, which is the change in the degree of anisotropy between room temperature (RT) and at 77 K (−196.15 °C; Schmidt et al., 2007). Biedermann et al. (2014) compiled p_{77} values for single crystal biotite (~12) and argued that the p_{77} value in a rock reveals the carrier of AMS. For example, the magnetic fabrics in a rock with p_{77} similar to single crystal biotite are attributed to biotite. Comparison of the p_{77} with those reported for biotite by Biedermann et al. (2014) reveal its contribution in the AMS.

$$p_{77} = \frac{K_{1(77\ \mathrm{K})} - K_{3(77\mathrm{K})}}{K_{1(\mathrm{RT})} - K_{3(\mathrm{RT})}}$$

LT-AMS of three specimens (2.6, 4.6, and 5.8) was measured at low temperature by cooling them with liquid nitrogen in KLY-4S Kappabridge (AGICO). These particular samples were selected because they present the highest magnetic susceptibility among all unshocked specimens (2.6), specimens that are shocked with the impact parallel with the foliation (4.6; Experiment A38), and perpendicular to the foliation (5.8; Experiment A37). The methodology is detailed in Issachar et al. (2016).

3. Results

3.1. Crater Morphology

The crater formed in Experiment A38, with the impact parallel to the foliation is smaller and shallower than in Experiment A37, with the impact perpendicular to the metamorphic foliation. Craters in A38 and A37 are 1.4 and 1.8 cm deep and on average 7.1 and 8.5 cm in diameter, respectively (Figure 1). The crater in A38 has partly steeper walls, compared to A37. The latter has a stepped cross-sectional profile. The depth to diameter (d/D) ratio is 0.20 and 0.21 for A38 and A37, respectively.

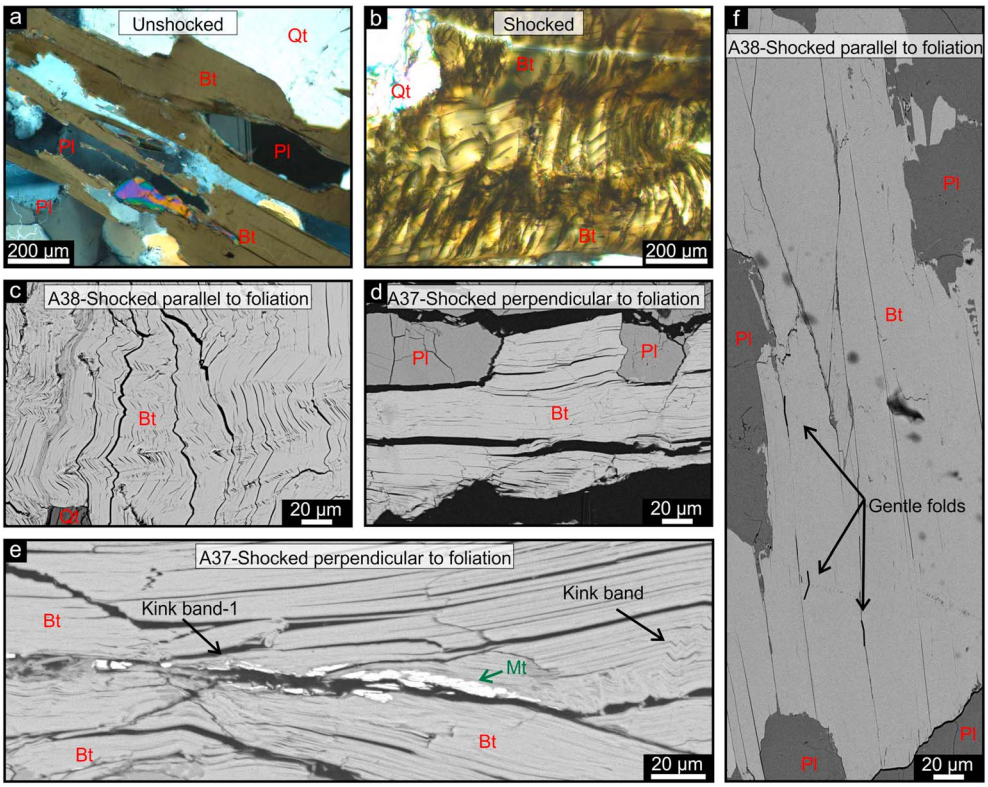

Figure 3. Cross-polarized photomicrographs and back scattered electron images, oriented perpendicular to the metamorphic foliation, elucidate impact effects on biotite. (a) Bands of undeformed biotite (Bt) are bordered on either side by lighter bands of plagioclase (Pl) and quartz (Qt). (b) The deformation due to impact cratering is realised as intense kinking in the biotite (Bt). (c and d) The intensity of kinking is much higher in the case where the impact direction is parallel to the foliation compared to an impact direction perpendicular to the foliation. Both back scattered electron images are taken at the crater floor. (e) The kink bands in biotite (Bt) and the fracture change the position of magnetite (Mt) grains, with respect to each other. (f) Biotite (Bt), 2.5 cm below the crater floor of A38, demonstrating several gentle folds, but no kink bands.

The calculated equivalent depth of burst, the point source, is defined as

$$d_b = d_p \sqrt{\frac{\rho_p}{\rho_t}},$$

where d_p is the projectile diameter, ρ_p is the projectile density, and ρ_t is the target density (Birkhoff et al., 1948). The point source of the shock waves is calculated to be at a depth of 5 mm for both experiments. For peak shock pressures calculation see supporting information (Ahrens & Johnson, 1995; Melosh, 1989; Perret & Bass, 1975).

3.2. Microscopic Observations

Maggia gneiss has alternating light and dark colored bands of quartz-feldspar and biotite, respectively (Figure 3a). The most obvious indicator of the impact are the kink bands in biotite, which are spread around the crater floor (Figures 3b–3d). Kinking is more prominent below both crater than at the sides. It is much more intense in A38, impacted parallel to the foliation, than in A37, impacted perpendicular to the foliation (Figures 3c and 3d). Kink folds near the crater floor are tighter, while those at greater depth are more open. The intensity of kink bands decreases with depth below the crater floor. In A37 the kinks are concentrated down to a depth of 1 cm (2 d_p) below the crater floor, while in A38 they are spread down to 2.1 cm (4.2 d_p). Further below some biotite grains are folded into gentle open folds with sporadic kink bands (Figure 3f). Before the impact the biotite grains present a strong preferred orientation, ~70% are vertical (Figure 4).

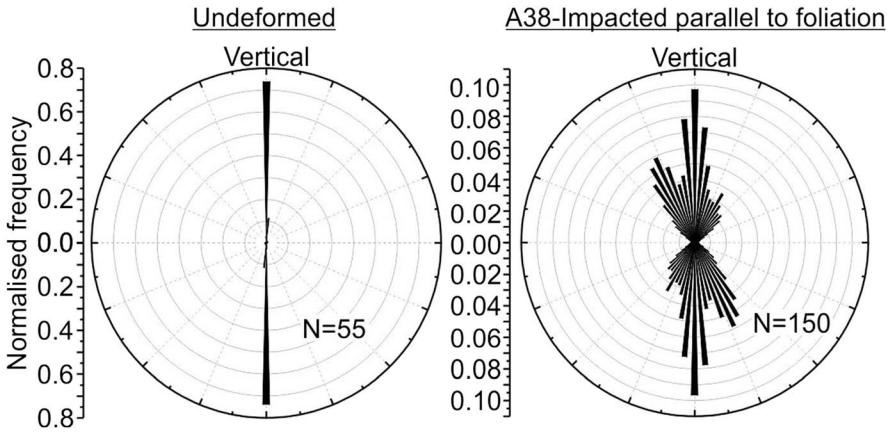

Figure 4. Rose plots present the variation in the orientation of the biotite long axis before and after impact. When undeformed >70% of the axis are orientated vertical; while in A38 <10% are vertical.

After the impact the kinking led to a spread in the orientation of the biotite long axes with <10% in the vertical direction (Figure 4).

In sample A38, impact parallel to the foliation, a large tensile fracture runs across the sample through the center of the crater subsurface, along the foliation (Figure 1). In the region down to ~1 cm below the crater floor, numerous smaller tensile fractures (<50 μm wide) traverse parallel and across to the foliation. In A37 tensile fractures are less frequent, most occurring along the foliation. In both cases (A38 and A37), the fractures cut across kink bands in the biotite and are therefore owed to the tensile pulse from the rarefaction wave. Winkler et al. (2018) labeled this region as "the zone of tensile failure." The kinking and the fractures affect the spatial distribution of the slightly elongated (~10 μm) magnetite grains by passively changing their position with respect to each other, for example, *Kink band-1* in Figure 3e.

3.3. Magnetic Carriers

In the unshocked sample (1.1), the bulk susceptibility at RT is 1.061×10^{-3} SI. The low-temperature part of the κ-T curve reveals a small but conspicuous peak at about −147 °C, representing the Verwey transition due to small amounts of almost pure magnetite (Tv in Figure 5a). The peak at the beginning of the curve, at about −194 °C, is an artifact. The heating branch of the high-temperature experiment shows considerable noise in the signal and a clear decrease in magnetic susceptibility at ~576 °C marking the Curie temperature of almost pure magnetite. There may be another subtle Curie transition at ~350 °C. But the signal is weak, and a confident determination of the magnetic mineral is difficult. The heating and cooling branches are comparable demonstrating a good reversibility, indicating the stability of the magnetite. The 350 °C signal is absent in the cooling curve and not stable upon heating. The ferromagnetic contribution in the bulk

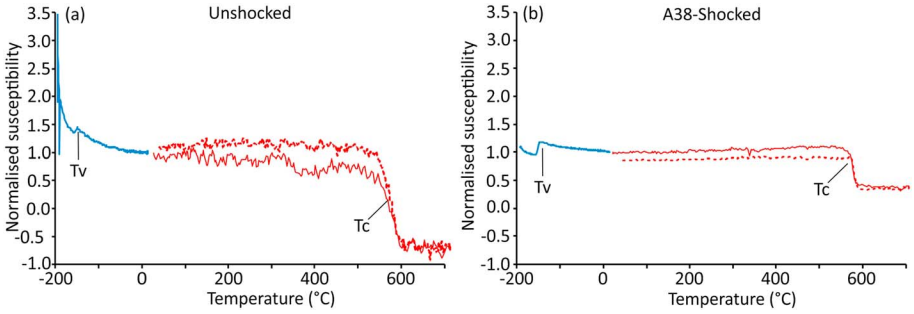

Figure 5. Thermomagnetic (κ-T) curve of (a) unshocked (specimen 1.1) and (b) shocked (specimen 4.1) gneiss showing the variation of normalised magnetic susceptibility with temperature, and the Verwey transition (Tv) and Curie temperature (Tc). The blue solid line represents the low-temperature measurement (−194 to 15 °C), while the red solid and dashed lines represent the heating and cooling branches of the high-temperature measurement (27.5 to 714 °C), respectively.

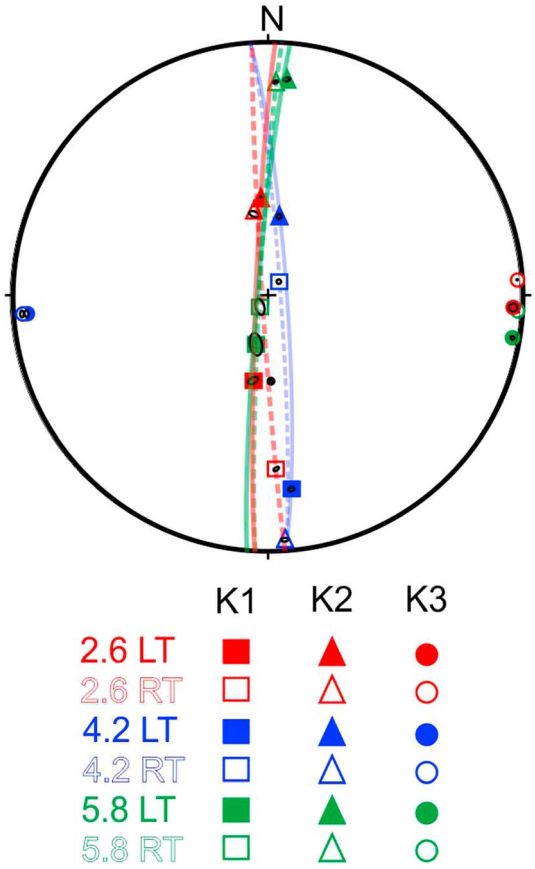

Figure 6. Lower hemisphere stereographic projection of the maximum (K1), intermediate (K2), and minimum (K3) susceptibility axis of specimen 2.6 (unshocked), 4.2 (A38-impacted parallel with the foliation), and 5.8 (A37-impacted perpendicular to the foliation) at RT and at −196.15 °C (LT). The confidence ellipse is also shown.

magnetic susceptibility is calculated to be 69.0 ± 0.5% using the hyperbola fitting in the Cureval8 software (AGICO). Note that these contributions refer to the bulk magnetic properties and do not refer to the ferromagnetic and paramagnetic contributions to AMS.

In the impacted sample (4.1 of A38) the bulk susceptibility (2.306×10^{-3} SI) at RT is higher than in the unshocked sample. In the low-temperature part a peak at −147 °C represent the Tv (Figure 5b). The heating and cooling branch of the high-temperature experiment have less noise than in the unshocked samples and a marked decrease in magnetic susceptibility at ~579 °C, which is the Curie temperature of almost pure magnetite. The normalized susceptibility in the unshocked sample falls to negative beyond 579 °C, indicating absence of any ferromagnetic phases with higher T_C. The less noisy curves of the shocked sample indicate higher magnetite content after impact experiment. Note that no additional phase at ~350 °C occur in the shocked sample.

The orientation of the K1, K2, and K3 of three specimens at RT and at low temperature (LT) are projected in lower hemisphere stereograph (Figure 6). All LT-K3 and the LT-magnetic foliation planes coincide with RT-K3 and the RT-magnetic foliation planes (Figure 6), indicating no difference in the orientation at room and low temperature. Biotite crystals exhibit a p_{77} usually between 11.98 and 12.41 (Biedermann et al., 2014). However, in the present case, p_{77} is 1.0, 0.939, and 1.01 for specimen 2.6, 4.2, and 5.8, respectively, indicating that the magnetic fabric is predominantly carried by magnetite. The ferrimagnetic fabric is coaxial with biotite fabrics (cf. Figures 4 and 6).

3.4. Magnetic Fabrics

3.4.1. Unshocked Magnetic Fabrics

The minimum principal susceptibility axes (K3) are well clustered (Figure 7). The unshocked Set 1 (specimens 1.1 to 1.10) and Set 2 (specimens 2.1 to 2.8) demonstrate a confidence ellipse of 1.8 and 1.7, respectively. The relative orientation of the K1, K2, and K3 indicate that the fabric is triaxial (e.g., Borradaile & Henry, 1997). At RT, unshocked gneiss have *Km* in the paramagnetic and para + ferrimagnetic range (0.376×10^{-3} SI to 1.298×10^{-3} SI). The corrected degree of anisotropy (P') varies between 1.32 and 1.94 (average = 1.49). P' of biotite single crystal is <2 (e.g., Borradaile & Werner, 1994; Zapletal, 1990). The shape parameter (T) is 0.5–0.72, average = 0.66 indicating oblate magnetic fabrics (supporting information Table S1). In the unshocked sample Sets 1 and 2, P' increases with *Km* (Figure 8). On the other hand, T does not show any correlation with P' (Figure 8).

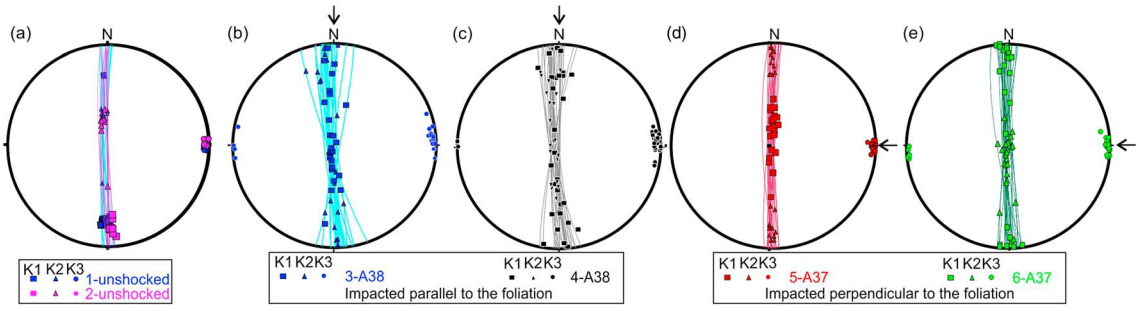

Figure 7. (a–e) Lower hemisphere stereographic projection of the magnetic fabrics of the unshocked and shocked specimens. The squares, triangles, and circles represent the maximum (K1), intermediate (K2), and minimum (K3) principal susceptibility axes, respectively. The great circles represent the magnetic foliation, and black arrows mark the impact direction.

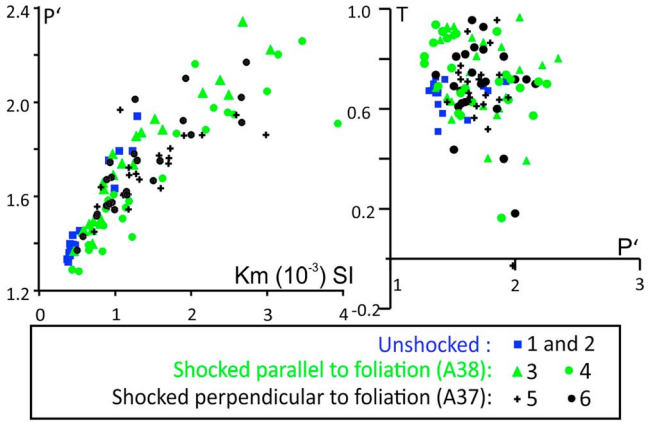

Figure 8. Jelinek's graphs after Jelinek (1981) showing the variation of corrected anisotropy (P'), shape parameter (T), and mean susceptibility (Km).

3.4.2. Shocked Magnetic Fabrics

The shocked samples (Sets 3 and 4 from A38 and 5 and 6 from A37) show a direct correlation between P' and Km, and no correlation between T and P' (Figure 8). Km varies from 0.464×10^{-3} SI to 3.940×10^{-3} SI (average at 1.47×10^{-3} SI) in A38 and from 0.508×10^{-3} SI to 2.992×10^{-3} SI (average at 1.49×10^{-3} SI) in A37 (supporting information Table S1). In samples from the block impacted parallel to the foliation, A38, P' and T vary between 1.28–2.34 (average = 1.72) and 0.16–0.96 (average = 0.73), respectively (Figure 8). In samples from the block impacted perpendicular to the foliation, A37, P' and T vary between 1.37 to 2.17 (average = 1.72) and −0.03 to 0.96 (average = 0.68), respectively (Figure 8). The shocked specimens, therefore, present increased the degree of anisotropy (P') and the bulk susceptibility (Km). The shock has increased the variability of magnetic fabrics with confidence ellipse between 0.1 and 2.5 (supporting information Table S1).

The shocked magnetic fabrics are oblate ($T > 0$, Figure 8 and supporting information Table S1), their orientation is, thus, reported and discussed in terms of the minimum principal susceptibility axis (K3), which is the pole to the foliation. The dispersion in K3 is represented with maps of plane and section view from A38 and A37 (Figure 9). It is presented with respect to the specimen farthest from the impact crater in each map. The plane view maps parallel to the target surface are at depth of 7 and 21 mm from the surface, and the section view maps are offset by 7 and 21 mm from the crater center. This coincides with the center of the first set of specimens (14 mm long) drilled at the surface (target and sawed surface) and the second set of specimens (14 mm long) drilled below the first set.

In A38, impacted parallel to the foliation, the plane view 7 mm (1.4 d_p) below the surface reveals a small zone near the impact crater with K3 deviating >14° (yellow zone in Figure 9a). K3 deviates 4° to 8° up to ~90 mm (18 d_p) away from the point source (yellow zone in Figure 9a). The zone of deviation shrinks at the depth of 21 mm (4.2 d_p) and is slightly stretched along the foliation, Y axis (yellow zone in Figure 9b). In the section view of A38, a ~30-mm-wide zone of high K3 deviation (10° to 22°), stretches down to 100 mm (20 d_p) below the point source along the foliation (yellow zone in Figure 9c). Deviation in K3 decreases sharply on either side of this zone. This region is thinner (15–20 mm) in the section with 21-mm offset from the crater center (yellow zone in Figure 9d). To generalize, in A38 (Figures 9a–9d), the deviation in K3 is more significant (up to 22°) when the shock waves propagate along the magnetic foliation. Whereas K3 deviates <4° for an oblique incidence of the shock wave. These deviations are statistically significant because the confidence ellipse is small (≤0.9°).

In the plane view of A37, 7 mm (1.4 d_p) below the surface, K3 variation is ≤8° up to ~70 mm (14 d_p) from the point source and decreases further away (Figure 9e). The scenario is more interesting in the plane view at depth of 21 mm (4.2 d_p) and in both section views (Figures 9f–9h). Here the maximum deviation of ~8° is concentrated along three edges of the map, except the edge farthest from the point source. Thus, the deviation in K3 reaches a maximum along a profile that runs about 45° to the impacted surface. In A37, vertically below the point of impact is a region of low deviation. This is in stark contrast to A38 where the highest deviation was measured in the vertical profile beneath the crater.

A comparison of all six maps reveals that in both A38 and A37 the zone of significant K3 deviation (area in yellow in Figure 9) is spread over a larger area in section view than in the plane view. The comparisons also reveal that the zone of K3 deviations is thinner in the section view with 21-mm offset than in section view with 7-mm offset because the former is farther from the point sources, and thus, the shock waves are weaker. These deviations are statistically significant because the confidence ellipse is small (≤2.5°).

To better appreciate the dispersion in K3 with distance from the point source, K3 of specimens in each radial profile of A38 were projected on a lower hemisphere stereonet. Three examples are presented in Figure 10, where each stereo net represents one individual profile. Out of the 16 profiles investigated, 12 present a systematic shift in K3 with decreasing distance from the point source. In the other four profiles, the shift is either not systematic or inconspicuous.

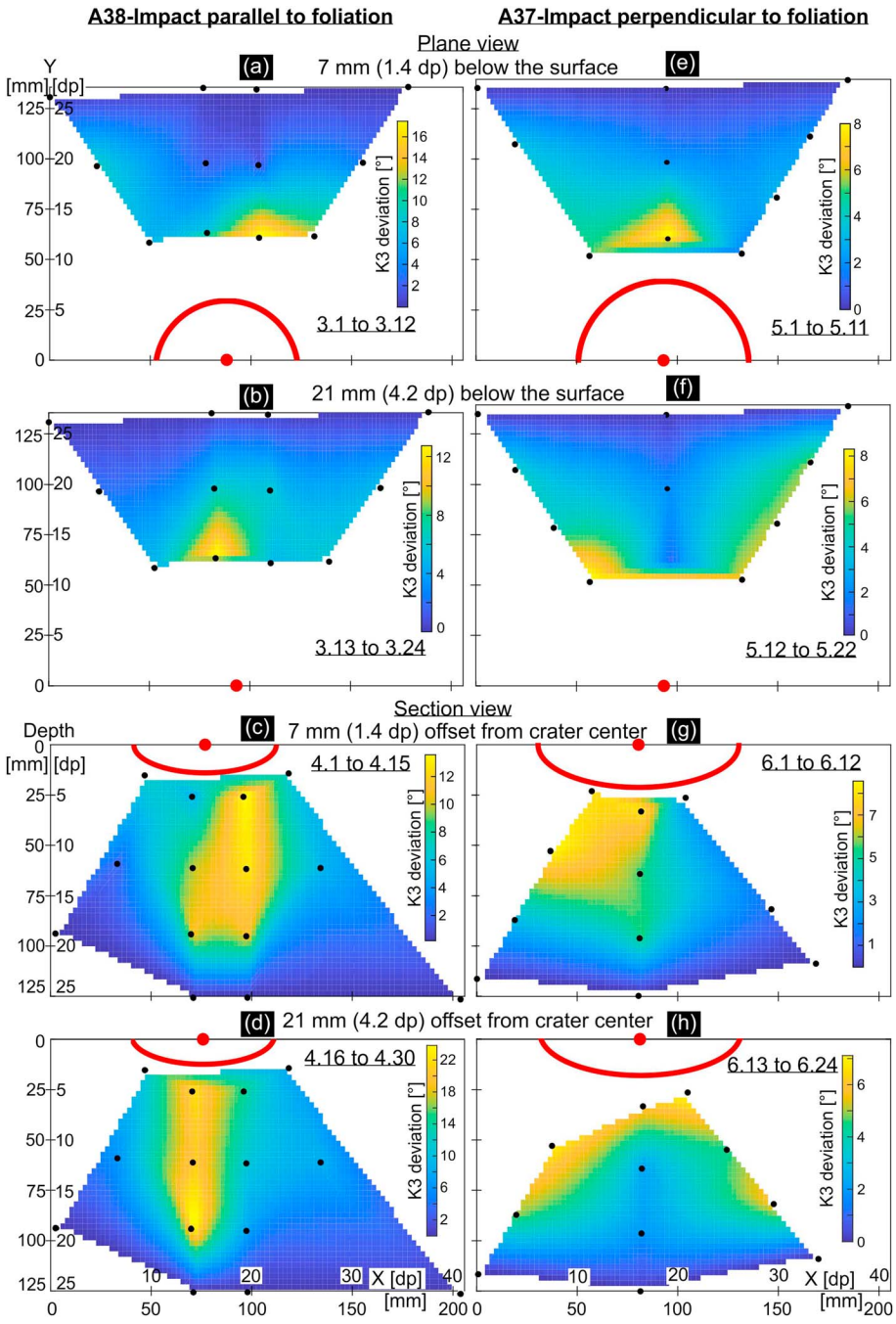

Figure 9. The maps show the position of the specimens (black dots) and the variation in the orientation of K3 with distance from the point source in sample (a–d) A38 (impacted parallel to the foliation) and (e–h) A37 (impacted perpendicular to the foliation). The impact crater is represented with red arc, and the point source is marked by a red dot. The metamorphic foliation is vertical striking along the *Y* axis in A38 and is horizontal in case of A37. The plane view maps are horizontal cuts at depths of 7 and 21 mm below surface marking the centre of the upper and lower set of specimens. The section view maps are vertical cuts with 7- and 21-mm offset from the crater center, corresponding to the center of the upper and lower set of specimens. Note that the plane view at 21-mm depth shows no crater, as the crater is shallower. The scale is shown millimetre (mm) and as well as projectile diameter [d_p]. See supporting information Figure S3 for sampling description.

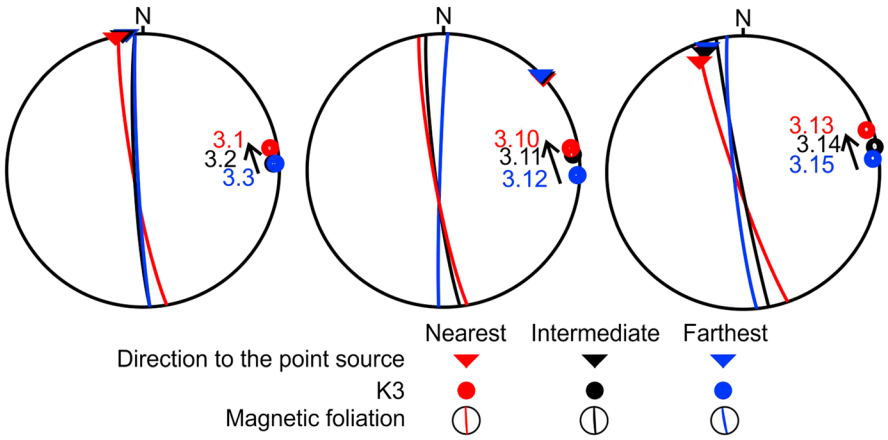

Figure 10. Three lower hemisphere stereo net projection of the minimum principal susceptibility axis K3 (circle), the magnetic foliation (arc), and the direction to the point source (triangle) present examples of reorientation of the magnetic fabrics and K3 in three radial profiles. In each profile, the specimen closest, intermediate, and farthest to the point source is represented in red, black, and blue, respectively. The reorientation of the K3 is demonstrated with a black arrow.

The K3 usually moves systematically either toward the impact or away from the impact with decreasing distance from the point source (Figure 10). In some cases, this decrease in distance is accompanied with, first, a slight and thereafter with a much more significant reorientation of K3. For example, K3 of 3.13 is farther away from K3 in 3.14, than the latter is from 3.15 (Figure 10). This is owed to the exponential increase in the peak shock intensity with a decrease in distance from the point source (Figure S1).

4. Discussion

Among the few available studies of the shock effect on magnetic fabrics (Gattacceca et al., 2007; Nishioka et al., 2007), none deals with phyllosilicate-bearing rocks or provide a systematic view of variation in AMS orientation in the subsurface of an impact crater. Two hypervelocity impact cratering experiments were done on Maggia gneiss blocks, shot parallel and perpendicular to the foliation. In both cases, impact was parallel to one principal axis of the magnetic fabrics; however, such parallelism is seldom in natural impacts. Further studies would need to incorporate additional geometries, that is, impact oblique to existing magnetic or petrofabric. The target rocks in the subsurface of the two craters experience low shock pressures (<2 GPa), which falls in S0–S1 of the typical shock stage classification (Stöffler, 1971; Stöffler et al., 2018). Typically, at such low pressures shock indicators and barometers are not well constrained. Shock barometers are better established for higher shock pressures, for example, to those corresponding with stages S2 (45 GPa) or S3 (51 GPa). AMS investigations presented in this study may aid in establishing shock barometers at low pressures. Our AMS results reveal a significant reorientation of K3, a marked increase in magnetic susceptibility, and in the degree of anisotropy due to weak shock pressures. Microscopic lines of evidence constrain the shift to deformation (kinking and fracturing) in biotite, which passively rotate and translate the magnetite grains (Figure 3e).

4.1. Effect of Shock Waves on Magnetic Properties

Impact cratering has led to a marked increase in average susceptibility from 0.61×10^{-3} SI (in unshocked specimens) to 1.47×10^{-3} SI (in A38) and 1.49×10^{-3} SI (in A37). But the magnetic susceptibility shows no relation with distance from the point source. This is contradictory to previous reports. At higher shock pressures >5 GPa, the ferrimagnetic susceptibility decreases with increasing shock pressure (e.g., Kontny & Grothaus, 2017; Nishioka et al., 2007; Reznik et al., 2016). Reznik et al. (2016) owe the decrease in susceptibility to fracturing (~5 GPa) and plastic deformation (>10 GPa).

Moreover, P' has increased from 1.49 to 1.72. Notably, the increase in average P' with impact parallel to the foliation is the same as the increase with impact perpendicular to the foliation. Increase in anisotropy is also reported from impact experiments on ferrimagnetic basalt and is owed to the fracturing of the magnetic grains at higher shock pressures >3 GPa (Gattacceca et al., 2007; Nishioka et al., 2007).

In the present case the peak shock pressure is low <2 GPa, which is below the Hugoniot elastic limit of magnetite (~5.0 GPa; Ahrens & Johnson, 1995). We cannot report on the deformation in magnetite grains, which might cause the increase in magnetic susceptibility and P'. Formation of new magnetite at mechanical heterogeneity such as cleavage or kink planes in biotite and transformation of Fe oxides/hydroxides into magnetite cannot be excluded. Lithological interfaces, for example, due to foliation, may lead to shock pressure excursions, additional accumulated strain, and localized shear displacements as observed at the microscale (Agarwal, Reznik, Alva-Valdivia, & Srivastava, 2016; Agarwal, Reznik, Kontny, et al., 2016) and in the field (Kenkmann & Ivanov, 2006).

On average, the shocked fabrics tend to be more oblate (average $T = 0.73$ for A38 and 0.68 for A37) than the unshocked fabrics (average $T = 0.66$). The impact process has thus flattened the magnetic fabrics. This is also evident from the change of triaxial K1, K2, and K3 in unshocked to K1–K2 forming a girdle in the shocked sample (Figure 7).

4.2. Deformation in Biotite and Reorientation of the Magnetic Fabrics

In A38 the degree of K3 deviation (dispersion) increases with vicinity to the point source, which is accompanied by an increase in peak shock pressure (Figures 9c and 9d). This decreasing distance to the point source is marked by an increase in fracturing, and by gentle folding at first, followed by kinking (Figure 3). This has two implications. First, the deformation in biotite will affect its crystallographic preferred orientation, leading to a higher variability in orientation of its long axis after the impact experiment (<10% remain vertical in Figure 4). The fracturing and kinking in biotite rotate the magnetite grains and change their position with respect to each other (Figure 3e). This affects the anisotropy from shape preferred orientation of elongate magnetite grains and the distribution anisotropy related to magnetite, thus affecting the magnetic fabrics. As the biotite crystallographic preferred orientation is more dispersed after the impact and affects the magnetic fabrics, the latter are also more dispersed after impact with confidence ellipse of K3 increasing from 0.6 before impact to 2.5 after impact (supporting information Table S1).

Second, Agarwal et al. (2019) report that in A38, biotite beneath the impact point source shows compressive strains >20% near the crater floor. With increasing depth beneath the surface, strain values decrease, and at 4 cm or 8 d_p distance from the crater floor, shortening has decreased by almost 2 orders of magnitude to ~0.1%. The decrease in kink intensity with distance from the point source, observed in present study may thus be correlated with the decrease in peak shock pressure and in compressive strain.

4.3. Intensity of Magnetic Fabric Reorientation in Crater Subsurface

The deviation in K3 is more significant (up to 22°) when the shock waves propagate along the magnetic foliation, whereas K3 deviates <4° for an oblique incidence of the shock wave. As a consequence, in A38 the maximum deformation is concentrated beneath the crater center, while in A37 it is along the sides (yellow zones in Figure 9). Along the center of A38, the shock wave moves subparallel to the foliation and to the basal planes of the biotite flakes. Biotite deforms more easily along the basal plane. The anisotropic strength of biotite causes buckling instabilities leading to the formation of kink bands (Chao, 1967; Cummings, 1965; Fel'dman et al., 2006; Gibson & Reimold, 2005; Hörz, 1969; Hörz & Ahrens, 1969; Schneider, 1972). In A37, regions with an oblique incidence of the shock wave, even if located farther away from the point source, show higher K3 deviation compared to regions with normal incidence nearer to the point source (yellow zones in Figure 9). This is because the oblique incidence results in a lower incident angle with respect to the biotite basal plane causing higher deformation, compared to a normal incidence. To summarize, the angularity between the incident shock wave and the foliation may have a greater consequence than the distance from the impact crater.

In both A38 and A37, the surface parallel sections present lesser deviation in K3 than the vertical sections, evident from a smaller zone of K3 reorientation (areas in yellow in Figure 9). This in principal agrees with numerical models, which show a higher magnitude of shock below the impact crater compared to the sides, where interference with the free surface leads to a lowering of the magnitude of the shock wave (e.g., Pierazzo & Melosh, 2000).

In some radial profiles of A38 (shocked parallel to the foliation) K3 reorients slightly at first and then significantly, with a decrease in distance from the point source. This probably goes along with the exponential increase in the peak shock pressure with the decreasing distance from the point source. The absence of

similar pattern in other profiles of A38 is owed, in part to the oblique incidence of the shock wave and in part to the distance of the specimens from the point source. The absence of pattern in A37 is owed to the impact being perpendicular to the foliation.

Reorientation of magnetic fabrics has been reported from other experimental impact studies. The reorientation of K3 toward the shock direction in A38 (foliation parallel to impact), reported here, is in accordance with the results of Gattacceca et al. (2007) on magnetite, Ti-magnetite, and pyrrhotite bearing rocks. However, present results disagree with Nishioka et al. (2007), who report alignment of K1 at 0.5–3 GPa in Ti-magnetite bearing andesitic basalt from Lonar crater, India. This disagreement may be due to the fact that these basalts possess both normal and inverse magnetic fabrics (Agarwal, Kontny, Srivastava, & Greiling, 2016). Gattacceca et al. (2007) attribute alignment of K3 to fracturing and/or dislocations of the ferromagnetic grains. However, rocks in the target subsurface of A37 and A38 experienced peak shock pressures <2 GPa, which is below the Hugoniot elastic limit of magnetite (~5.0 GPa; Ahrens and Johnson), although tensile fractures formed during decompression of the wave may have also affected the magnetite grains (Figure 3e). AMS investigations on phyllosilicate-bearing rocks deformed in tectonic regimes attribute reorientation of K3 to shearing and folding of paramagnetic minerals, such as biotite and chlorite, in response to the tectonic stresses, which is partly similar to the present situation (e.g., Borradaile & Henry, 1997; Borradaile & Jackson, 2010; Hrouda, 1982; Joshi et al., 2017; Martín-Hernández & Hirt, 2004; Tarling & Hrouda, 1993).

5. Conclusions

This study investigates changes in the AMS signature of a foliated, biotite-rich gneiss affected by impact cratering. An increase in corrected magnetic anisotropy P' and bulk susceptibility is observed at lower peak shock pressures than was previously reported. In both experiments, A38 (impact direction parallel to the foliation) and A37 (impact direction perpendicular to the foliation), the minimum principal magnetic susceptibility axis, K3, reorients more intensely beneath the crater than adjacent to it. The strongest reorientation occurs when the shock wave propagation direction parallels the (001) planes of biotite.

AMS of magnetic fabric is already an established technique for understanding impact processes, especially at low peak shock pressures (0.5 to 3 GPa), at which other common shock indicators are rare (e.g., Agarwal et al., 2015; Agarwal, Kontny, Srivastava, & Greiling, 2016; Misra et al., 2010; Stöffler et al., 2018). The present study concludes that folding and kinking of biotite due to shock deformation may cause a significant reorientation of magnetic fabrics by passively changing the position of magnetite grains with respect to each other. Reorientation of magnetic fabrics is conspicuous down to 20 d_p (10 cm) below the point source. No other impact related deformation is visible at this depth. The reorientation of magnetic fabrics may, therefore, aid in identifying impact processes at very low peak shock pressures >0.1 GPa, when other common indicators are absent. In agreement, Gattacceca et al. (2005) propose that up to shock stage S3, AMS may be more precise than microscopy observations that provide information only on a limited surface, contrary to the volume information provided by magnetic measurements.

Acknowledgments
The Alexander von Humboldt Foundation is thanked for the postdoctoral fellowship to A. A. The experiments have been conducted in the framework of the research unit FOR-887, MEMIN, the Multidisciplinary Experimental and Modeling Impact research Network, financed by the Deutsche Forschungsgemeinschaft DFG, Grant KE 732/16-2. We are grateful to the technicians of the Ernst-Mach-Institute for conducting the shots. Research Innovation Fund of the University of Freiburg is thanked for further financial support. Matthias Ebert is thanked for additional SEM and EDS measurements. Jacob Wilk is thanked for preparation of the maps showing variation in the orientation of K3. Stephen Parman, Mark Dekkers, Adrian Muxworthy and two other anonymous reviewers are thanked for their suggestions during the review process. All of the data on which this manuscript is based are provided in the supporting information.

References

Agarwal, A., Kontny, A., & Greiling, R. O. (2015). Relationships among magnetic fabrics, microfractures and shock pressures at an impact crater: A case study from Lockne crater, Sweden. *Journal of Applied Geophysics*, *114*, 232–243. https://doi.org/10.1016/j.jappgeo.2015.01.010

Agarwal, A., Kontny, A., Srivastava, D. C., & Greiling, R. O. (2016). Shock pressure estimates in target basalts of a pristine crater: A case study in the Lonar crater, India. *Geological Society of America Bulletin*, *128*(1-2), 19–28. https://doi.org/10.1130/B31172.1

Agarwal, A., Poelchau, M.H., Kenkmann, T., 2019. Kinked biotite as a strain marker in experimental impact craters in gneiss. in: Lunar and Planetary Science Conference.

Agarwal, A., Reznik, B., Alva-Valdivia, L. M., & Srivastava, D. C. (2016). Alternating augite-plagioclase wedges in basement dolerites of Lockne impact structure, Sweden: A new shock wave-induced deformation feature. *Meteoritics and Planetary Science*, *52*(3), 458–470. https://doi.org/10.1111/maps.12806

Agarwal, A., Reznik, B., Kontny, A., Heissler, S., & Schilling, F. (2016). Lingunite-a high-pressure plagioclase polymorph at mineral interfaces in doleritic rock of the Lockne impact structure (Sweden). *Scientific Reports*, *6*(1), 25991. https://doi.org/10.1038/srep25991

Ahrens, T. J., & Johnson, M. L. (1995). Shock wave data for rocks. In *A Handb. Phys. Constants*, *Miner. Phys. Crystallogr* (Vol. 3, pp. 35–44). Washington, DC: American Geophysical Union.

Alvarez, L. W., Alvarez, W., Asaro, F., & Michel, H. V. (1980). Extraterrestrial cause for the cretaceous-tertiary extinction. *Science*, *208*(4448), 1095–1108. https://doi.org/10.1126/science.208.4448.1095

Biedermann, A. R., Bender Koch, C., Lorenz, W. E. A., & Hirt, A. M. (2014). Low-temperature magnetic anisotropy in micas and chlorite. *Tectonophysics*, *629*, 63–74. https://doi.org/10.1016/j.tecto.2014.01.015

Birkhoff, G., MacDougall, D. P., Pugh, E. M., Taylor, G., & Taylor, S. G. (1948). Explosives with lined cavities. *Journal of Applied Physics*, *19*(6), 563–582. https://doi.org/10.1063/1.1698173

Borradaile, G. J., & Henry, B. (1997). Tectonic applications of magnetic susceptibility and its anisotropy. *Earth-Science Reviews*, *42*(1-2), 49–93. https://doi.org/10.1016/S0012-8252(96)00044-X

Borradaile, G. J., & Jackson, M. (2010). Structural geology, petrofabrics and magnetic fabrics (AMS, AARM, AIRM). *Journal of Structural Geology*, *32*(10), 1519–1551. https://doi.org/10.1016/j.jsg.2009.09.006

Borradaile, G. J., & Werner, T. (1994). Magnetic anisotropy of some phyllosilicates. *Tectonophysics*, *235*(3), 223–248. https://doi.org/10.1016/0040-1951(94)90196-1

Chao, E. C. T. (1967). Shock effects in certain rock-forming minerals. *Science*, *156*(3772), 192–202. https://doi.org/10.1126/science.156.3772.192

Cowan, E. J. (1999). Magnetic fabric constraints on the initial geometry of the Sudbury Igneous Complex: A folded sheet or a basin-shaped igneous body? *Tectonophysics*, *307*(1-2), 135–162. https://doi.org/10.1016/S0040-1951(99)00123-7

Cullity, B. D., & Graham, C. D. (2011). *Introduction to magnetic materials*. Hoboken, NJ: John Wiley & Sons.

Cummings, D. (1965). Kink-bands: Shock deformation of biotite resulting from a nuclear explosion. *Science*, *148*(3672), 950–952. https://doi.org/10.1126/science.148.3672.950

Delgadillo-Peralta, M., Urrutia-Fucugauchi, J., Pérez-Cruz, L., & Velasco-Villarreal, M. (2015). Rock magnetic and AMS fabrics characterization of suevitic breccias from the Cretaceous-Paleogene Chicxulub impact crater. *Revista Mexicana de Ciencias Geológicas*, *32*(1), 145–155.

Fel'dman, V. I., Sazonova, L. V., & Kozlov, E. A. (2006). Shock metamorphism of some rock-forming minerals: Experimental results and natural observations. *Petrology*, *14*(6), 540–566. https://doi.org/10.1134/S0869591106060038

French, B. M., & Koeberl, C. (2010). The convincing identification of terrestrial meteorite impact structures: What works, what doesn't, and why. *Earth-Science Reviews*, *98*(1-2), 123–170. https://doi.org/10.1016/j.earscirev.2009.10.009

Fritz, J., Greshake, A., & Fernandes, V. A. (2017). Revising the shock classification of meteorites. *Meteoritics and Planetary Science*, *52*(6), 1216–1232. https://doi.org/10.1111/maps.12845

Gattacceca, J., Lamali, A., Rochette, P., Boustie, M., & Berthe, L. (2007). The effects of explosive-driven shocks on the natural remanent magnetization and the magnetic properties of rocks. *Physics of the Earth and Planetary Interiors*, *162*(1-2), 85–98. https://doi.org/10.1016/j.pepi.2007.03.006

Gattacceca, J., Rochette, P., Denise, M., Consolmagno, G., & Folco, L. (2005). An impact origin for the foliation of chondrites. *Earth and Planetary Science Letters*, *234*(3-4), 351–368. https://doi.org/10.1016/j.epsl.2005.03.002

Gibson, R. L., & Reimold, W. U. (2005). Shock pressure distribution in the Vredefort impact structure, South Africa. In T. Kenkmann, F. Hörz, & A. Deutsch (Eds.), *Special Paper 384: Large Meteorite Impacts III*, (pp. 329–349). Boulder, USA: Geological Society of America. https://doi.org/10.1130/0-8137-2384-1.329

Grieve, R. A. F., Langenhorst, F., & Stöffler, D. (1996). Shock metamorphism of quartz in nature and experiment: II. Significance in geoscience*. *Meteoritics and Planetary Science*, *31*(1), 6–35. https://doi.org/10.1111/j.1945-5100.1996.tb02049.x

Hirt, A. M., Lowrie, W., Clendenen, W. S., & Kligfield, R. (1993). Correlation of strain and the anisotropy of magnetic susceptibility in the Onaping Formation: Evidence for a near-circular origin of the Sudbury Basin. *Tectonophysics*, *225*(4), 231–254. https://doi.org/10.1016/0040-1951(93)90300-9

Hörz, F. (1969). Structural and mineralogical evaluation of an experimentally produced impact crater in granite. *Contributions to Mineralogy and Petrology*, *21*(4), 365–377. https://doi.org/10.1007/BF02672808

Hörz, F., & Ahrens, T. J. (1969). Deformation of experimentally shocked biotite. *American Journal of Science*, *267*(10), 1213–1229. https://doi.org/10.2475/ajs.267.10.1213

Hrouda, F. (1982). Magnetic anisotropy of rocks and its application in geology and geophysics. *Geophysical Surveys*, *5*(1), 37–82. https://doi.org/10.1007/BF01450244

Hrouda, F. (1994). A technique for the measurement of thermal changes of magnetic susceptibility of weakly magnetic rocks by the CS-2 apparatus and KLY-2 Kappabridge. *Geophysical Journal International*, *118*(3), 604–612. https://doi.org/10.1111/j.1365-246X.1994.tb03987.x

Hrouda, F., Jelínek, V., & Zapletal, K. (1997). Refined technique for susceptibility resolution into ferromagnetic and paramagnetic components based on susceptibility temperature-variation measurement. *Geophysical Journal International*, *129*(3), 715–719. https://doi.org/10.1111/j.1365-246X.1997.tb04506.x

Issachar, R., Levi, T., Lyakhovsky, V., Marco, S., & Weinberger, R. (2016). Improving the method of low-temperature anisotropy of magnetic susceptibility (LT-AMS) measurements in air. *Geochemistry, Geophysics, Geosystems*, *17*, 2940–2950. https://doi.org/10.1002/2016GC006339

Jelinek, V. (1981). Characterization of the magnetic fabric of rocks. *Tectonophysics*, *79*(3-4), T63–T67. https://doi.org/10.1016/0040-1951(81)90110-4

Joshi, G., Agarwal, A., Agarwal, K. K., Srivastava, S., & Alva-Valdivia, L. M. (2017). Microstructures and strain variation: Evidence of multiple splays in the North Almora Thrust Zone, Kumaun Lesser Himalaya, Uttarakhand, India. *Tectonophysics*, *694*, 239–248. https://doi.org/10.1016/j.tecto.2016.11.008

Kapička, A. (1988). Anisotropy of magnetic susceptibility in a weak magnetic field induced by stress. *Physics of the Earth and Planetary Interiors*, *51*(4), 349–354. https://doi.org/10.1016/0031-9201(88)90075-1

Kenkmann, T., Deutsch, A., Thoma, K., Ebert, M., Poelchau, M. H., Buhl, E., et al. (2018). Experimental impact cratering: A summary of the major results of the MEMIN research unit. *Meteoritics and Planetary Science*, *53*(8), 1543–1568. https://doi.org/10.1111/maps.13048

Kenkmann, T., & Ivanov, B. A. (2006). Target delamination by spallation and ejecta dragging: An example from the Ries crater's periphery. *Earth and Planetary Science Letters*, *252*(1-2), 15–29. https://doi.org/10.1016/j.epsl.2006.08.024

Kenkmann, T., Poelchau, M. H., & Wulf, G. (2014). Structural geology of impact craters. *Journal of Structural Geology*, *62*, 156–182. https://doi.org/10.1016/j.jsg.2014.01.015

Kontny, A., & Grothaus, L. (2017). Effects of shock pressure and temperature on titanomagnetite from ICDP cores and target rocks of the El'gygytgyn impact structure, Russia. *Studia Geophysica et Geodaetica*, *61*(1), 162–183. https://doi.org/10.1007/s11200-016-0819-3

Kumar, P. S., & Kring, D. A. (2008). Impact fracturing and structural modification of sedimentary rocks at Meteor Crater, Arizona. *Journal of Geophysical Research*, *113*, E09009. https://doi.org/10.1029/2008JE003115

Mang, C., Kontny, A., Fritz, J., & Schneider, R. (2013). Shock experiments up to 30 GPa and their consequences on microstructures and magnetic properties in pyrrhotite. *Geochemistry, Geophysics, Geosystems*, *14*, 64–85. https://doi.org/10.1029/2012GC004242

Martín-Hernández, F., & Ferré, E. C. (2007). Separation of paramagnetic and ferrimagnetic anisotropies: A review. *Journal of Geophysical Research*, *112*, B03105. https://doi.org/10.1029/2006JB004340

Martín-Hernández, F., & Hirt, A. M. (2004). A method for the separation of paramagnetic, ferrimagnetic and haematite magnetic subfabrics using high-field torque magnetometry. *Geophysical Journal International*, *157*(1), 117–127. https://doi.org/10.1111/j.1365-246X.2004.02225.x

Melosh, H. J. (1989). *Impact cratering: A geologic process*, *Oxford Monographs on Geology and Geophysics*, (11th ed.. Research supported by NASAp. 253). New York: Oxford University Press.

Misra, S., Arif, M., Basavaiah, N., Srivastava, P. K., & Dube, A. (2010). Structural and anisotropy of magnetic susceptibility (AMS) evidence for oblique impact on terrestrial basalt flows: Lonar crater, India. *Bulletin Geological Society of America*, *122*(3-4), 563–574. https://doi.org/10.1130/B26550.1

Neukum, G., Ivanov, B. A., & Hartmann, W. K. (2001). *Cratering records in the inner solar system in relation to the lunar reference system, in: Chronology and evolution of Mars*, (pp. 55–86). Dordrecht: Springer.

Nishioka, I., Funaki, M., & Sekine, T. (2007). Shock-induced anisotropy of magnetic susceptibility: Impact experiment on basaltic andesite. *Earth, Planets and Space*, *59*(11), e45–e48. https://doi.org/10.1186/BF03352060

Perret, W. R., & Bass, R. C. (1975). *Free-field ground motion induced by underground explosions*, (p. 125). Albuquerque, N. Mex.(USA): Sandia Labs.

Pierazzo, E., & Melosh, H. J. (2000). Understanding oblique impacts from experiments, observations, and modeling. *Annual Review of Earth and Planetary Sciences*, *28*(1), 141–167. https://doi.org/10.1146/annurev.earth.28.1.141

Poelchau, M. H., Kenkmann, T., Thoma, K., Hoerth, T., Dufresne, A., & Schäfer, F. (2013). The MEMIN research unit: Scaling impact cratering experiments in porous sandstones. *Meteoritics and Planetary Science*, *48*(1), 8–22. https://doi.org/10.1111/maps.12016

Poelchau, M.H., Winkler, R., Schäfer, F., Kenkmann, T., 2016. Experimental Cratering into Layered Targets: MEMIN Experiments with Maggia gneiss, in: 79th Annual Meeting of the Meteoritical Society. Berlin, Germany, p. A1, doi:https://doi.org/10.1111/maps.12934, 52, A408

Reznik, B., Kontny, A., & Fritz, J. (2017). Effect of moderate shock waves on magnetic susceptibility and microstructure of a magnetite-bearing ore. *Meteoritics and Planetary Science*, *52*(7), 1495–1504. https://doi.org/10.1111/maps.12787

Reznik, B., Kontny, A., Fritz, J., & Gerhards, U. (2016). Shock-induced deformation phenomena in magnetite and their consequences on magnetic properties. *Geochemistry, Geophysics, Geosystems*, *17*, 2374–2393. https://doi.org/10.1002/2016GC006338

Schmidt, V., Hirt, A. M., Rosselli, P., & Martín-Hernández, F. (2007). Separation of diamagnetic and paramagnetic anisotropy by high-field, low-temperature torque measurements. *Geophysical Journal International*, *168*(1), 40–47. https://doi.org/10.1111/j.1365-246X.2006.03202.x

Schneider, E., & Schäfer, F. (2001). Hypervelocity impact research-acceleration technology and applications. *Advances in Space Research*, *28*(9), 1417–1424. https://doi.org/10.1016/S0273-1177(01)00448-3

Schneider, H. (1972). Shock-induced mechanical deformations in biotites from crystalline rocks of the ries crater (Southern Germany). *Contributions to Mineralogy and Petrology*, *37*(1), 75–85. https://doi.org/10.1007/BF00377308

Stöffler, D. (1971). Progressive metamorphism and classification of shocked and brecciated crystalline rocks at impact craters. *Journal of Geophysical Research*, *76*(23), 5541–5551. https://doi.org/10.1029/JB076i023p05541

Stöffler, D., Hamann, C., & Metzler, K. (2018). Shock metamorphism of planetary silicate rocks and sediments: Proposal for an updated classification system. *Meteoritics and Planetary Science*, *53*(1), 5–49. https://doi.org/10.1111/maps.12912

Stöffler, D., Hornemann, U., Stoeffler, D., & Hornemann, U. (1972). Quartz and feldspar glasses produced by natural and experimental shock. *Meteoritics*, *7*(3), 371–394. https://doi.org/10.1111/j.1945-5100.1972.tb00449.x

Stöffler, D., Keil, K., & Scott, E. R. D. (1992). Shock classification of ordinary chondrites: New data and interpretations. *Meteoritics*, *55*(12), 3845–3867. https://doi.org/10.1016/0016-7037(91)90078-J

Stöffler, D., & Langenhorst, F. (1994). Shock metamorphism of quartz in nature and experiment: I. Basic observation and theory*. *Meteoritics*, *29*(2), 155–181. https://doi.org/10.1111/j.1945-5100.1994.tb00670.x

Strom, R. G., Malhotra, R., Ito, T., Yoshida, F., & Kring, D. A. (2005). The origin of planetary impactors in the inner solar system. *Science*, *309*(5742), 1847–1850. https://doi.org/10.1126/science.1113544

Tarling, D., & Hrouda, F. (1993). *Magnetic anisotropy of rocks*, (pp. 95–160). Heidelberg, New York, Dordrecht, London: Springer.

Winkler, R., Luther, R., Poelchau, M. H., Wünnemann, K., & Kenkmann, T. (2018). Subsurface deformation of experimental hypervelocity impacts in quartzite and marble targets. *Meteoritics and Planetary Science*, *53*(8), 1733–1755. https://doi.org/10.1111/maps.13080

Yokoyama, E., Trindade, R. I. F., Lana, C., Filho, C. R. S., Baratoux, D., Marangoni, Y. R., & Tohver, E. (2012). Magnetic fabric of Araguainha complex impact structure (Central Brazil): Implications for deformation mechanisms and central uplift formation. *Earth and Planetary Science Letters*, *331-332*, 347–359. https://doi.org/10.1016/j.epsl.2012.01.005

Zapletal, K. (1990). Low-field susceptibility anisotropy of some biotite crystals. *Physics of the Earth and Planetary Interiors*, *63*(1-2), 85–97. https://doi.org/10.1016/0031-9201(90)90063-4